

Post-Annealing Treatment on Hydrothermally Grown Antimony Sulfoselenide Thin Films for Efficient Solar Cells


Suman Rijal, Alisha Adhikari, Rasha A. Awni, Chuanxiao Xiao, Deng-Bing Li, Briana Dokken, Anna Ellingson, Ernesto Flores, Sandip S. Bista, Dipendra Pokhrel, Sabin Neupane, Richard E. Irving, Adam B. Phillips, Katherine Jungjohann, Chun-Sheng Jiang, Mowafak Al-Jassim, Randy J. Ellingson, Zhaoning Song,* and Yanfa Yan*

Herein, antimony sulfoselenide ($\text{Sb}_2(\text{S}, \text{Se})_3$) thin-film solar cells are fabricated by a hydrothermal method followed by a post-deposition annealing process at different temperatures and the impact of the annealing temperature on the morphological, structural, optoelectronic, and defect properties of the hydrothermally grown $\text{Sb}_2(\text{S}, \text{Se})_3$ films is investigated. It is found that a proper annealing temperature leads to high-quality $\text{Sb}_2(\text{S}, \text{Se})_3$ films with large crystal grains, high crystallinity, preferred crystal orientation, smooth and uniform morphology, and reduced defect density. These results show that suppressing deep-level defects is crucial to enhance solar cell performance. After optimizing the annealing process, $\text{Sb}_2(\text{S}, \text{Se})_3$ solar cells with an improved power conversion efficiency 2.04 to 8.48% are obtained.

1. Introduction

Metal chalcogenide thin-film photovoltaics (PV) have experienced significant improvements in power conversion efficiencies (PCEs)

S. Rijal, A. Adhikari, R. A. Awni, D.-B. Li, B. Dokken, A. Ellingson, E. Flores, S. S. Bista, D. Pokhrel, S. Neupane, R. E. Irving, A. B. Phillips, R. J. Ellingson, Z. Song, Y. Yan
Wright Center for Photovoltaics Innovation and Commercialization
Department of Physics and Astronomy
The University of Toledo
Toledo, OH 43606, USA
E-mail: zhaoning.song@utoledo.edu; yanfa.yan@utoledo.edu
C. Xiao, K. Jungjohann, C.-S. Jiang, M. Al-Jassim
Materials Science Center
National Renewable Energy Laboratory
Golden, CO 80401, USA

 The ORCID identification number(s) for the author(s) of this article can be found under <https://doi.org/10.1002/solr.202201009>.

© 2022 The Authors. Solar RRL published by Wiley-VCH GmbH. This is an open access article under the terms of the Creative Commons Attribution License, which permits use, distribution and reproduction in any medium, provided the original work is properly cited.

The publisher acknowledges that the United States Government retains a non-exclusive, paid-up, irrevocable, world-wide license to publish or reproduce the published form of this article, or allow others to do so, for United States Government purposes only.

DOI: 10.1002/solr.202201009

and module production over the past decade. The commercial thin-film PV technologies based on cadmium telluride (CdTe) and copper indium gallium selenide (Cu(In, Ga)Se₂ or CIGS) achieved PCE records of 22.1%^[1] and 23.4%^[2] respectively. The global annual production of thin-film PV modules was approaching 8 GW in 2020.^[3] With an increasing demand for thin-film PV to realize net-zero carbon emissions in the near future, concerns have been raised regarding the scarcity of rare elements like Te, In, and Ga, and the toxicity of heavy metals like Cd.^[4] Recently, antimony chalcogenides, including antimony selenide (Sb_2Se_3), antimony sulfur (Sb_2S_3), and their alloy compounds,

antimony sulfoselenide ($\text{Sb}_2(\text{S}, \text{Se})_3$), have come out as promising alternatives for thin-film PV absorber materials, thanks to their appealing features, such as environmental friendliness, low toxicity, earth abundance, and ease of synthesis.^[5] This family of materials has a unique stibnite crystal structure featuring oriented 1D ribbon-type grains, electrically benign grain boundaries, and anisotropic optical and electrical properties.^[6,7] Additionally, $\text{Sb}_2(\text{S}, \text{Se})_3$ possesses a tunable bandgap of 1.03–1.8 eV by adjusting the S to Se ratio, outstanding absorption coefficients ($\approx 10^5 \text{ cm}^{-1}$), and robust material stability.^[8]

The performance of heterojunction antimony chalcogenide thin-film solar cells strongly depends on the quality of the absorber material. The desired properties of a high-quality thin-film absorber layer include high crystallinity, large grain size, uniform morphology, low defect density, suitable bandgap, long charge carrier lifetime, and fast charge carrier transport. The deposition method and post-deposition treatments largely determine the quality of the absorber layer. Antimony chalcogenide films can be fabricated by different routes, including spin coating,^[9] physical vapor deposition (PVD),^[10] sputtering,^[11] chemical bath deposition (CBD),^[12] hydrothermal approach,^[8a,13] and closed space sublimation (CSS).^[6,14] Among various methods, hydrothermal growth is a facile approach to deposit high-quality antimony selenide films with uniform morphology and homogeneous stoichiometry at low fabrication costs. However, the hydrothermal approach is fundamentally limited by the low thermal budget during the film growth, resulting

in low crystallinity and high defect density in the absorber layer. The as-deposited films typically suffer from high nonradiative recombination in bulk and at the interfaces, leading to poor PV performance. Despite these drawbacks, hydrothermally grown $\text{Sb}_2(\text{S}, \text{Se})_3$ solar cells have shown a promising PCE of 10.7% after tuning the absorber composition and employing post-deposition annealing.^[15] Particularly, post-deposition annealing is found to be effective in improving Sb_2Se_3 and Sb_2S_3 solar cells.^[6a,13b,14,16] Annealing provides a thermodynamic driving force to promote grain growth, reduce internal defects, release the internal stress of the film, and promote compactness and crystallization.^[17] The impact of post-annealing treatments on the performance of $\text{Sb}_2(\text{S}, \text{Se})_3$ thin-film solar cells has been studied previously. Wang et al. studied the post-selenization effect on $\text{Sb}_2(\text{S}, \text{Se})_3$ solar cells fabricated by a hydrothermal method.^[13b] Tang et al. realized a PCE of 10% for $\text{Sb}_2(\text{S}, \text{Se})_3$ solar cells by optimizing the S/Se ratio and post-annealing temperature.^[8a] Further, Zhao et al. studied the effect of an alkaline metal fluoride treatment on $\text{Sb}_2(\text{S}, \text{Se})_3$ films and an annealing process to regulate energy band alignment, enhancing the PCE of $\text{Sb}_2(\text{S}, \text{Se})_3$ solar cells to 10.7%.^[15] However, much of the previous research is descriptive in nature, providing incomplete information on the effect of post-annealing conditions on the physical properties, particularly defect properties of $\text{Sb}_2(\text{S}, \text{Se})_3$ films.

In this work, we demonstrate a facile hydrothermal method to prepare $\text{Sb}_2(\text{S}, \text{Se})_3$ thin films and investigate the impact of post-annealing temperature on the morphological, structural, optoelectronic, and defect properties of the $\text{Sb}_2(\text{S}, \text{Se})_3$ films. We find that $\text{Sb}_2(\text{S}, \text{Se})_3$ thin films annealed at 350 °C exhibit uniform surface morphology, larger crystal grains, preferred crystal orientation, and reduced defects, leading to a champion PCE of 8.48% in superstrate $\text{Sb}_2(\text{S}, \text{Se})_3$ solar cells. This device fabrication procedure is highly reproducible, allowing our undergraduate and high school student researchers to reproduce efficient thin-film solar cells.

2. Results and Discussions

Figure 1 shows the scanning electron microscopic (SEM) surface images of the ≈ 1.48 eV $\text{Sb}_2(\text{S}, \text{Se})_3$ thin films deposited by a hydrothermal method, followed by post-annealing in a tube furnace at different temperatures ranging from 300 to 400 °C for 10 min. The detailed fabrication procedure is provided in the Experimental Section and shown in Figure S1, Supporting Information. The hydrothermally grown $\text{Sb}_2(\text{S}, \text{Se})_3$ film consists of small and rounded grains with an average visual grain size of ≈ 300 nm (Figure 1a). After annealing the $\text{Sb}_2(\text{S}, \text{Se})_3$ films at elevated temperatures, the grains are coalesced and grown into large crystalline domains with obvious crystal facets and edges (Figure 1b–f). Despite increased grain sizes, increasing the annealing temperature leads to nonuniform morphology and microcracks and voids at the grain boundaries of the crystalline domains (Figure S2, Supporting Information), likely due to the evaporation of S and Se from the films and releasing stresses during thermal ramping. These microcracks with off-stoichiometric S/Se-poor compositions and structural defects are likely acting as recombination centers and shunting paths in solar cells due to a high density of dangling bonds and under-coordinated surface atoms, which eventually lower the device performance. The optical transmittance and absorbance spectra of the films annealed at different temperatures from 300 to 400 °C exhibit insignificant changes in the bandgap, whereas the unannealed film shows a much higher bandgap with a reduced absorption coefficient (Figure S3, Supporting Information). The results indicate a conversion from the as-deposited precursor phase to $\text{Sb}_2(\text{S}, \text{Se})_3$ after annealing. Among all samples, the $\text{Sb}_2(\text{S}, \text{Se})_3$ film annealed at 350 °C shows the best film quality in terms of the crystalline domain size, pin-hole-free and crack-less morphology, and high optical absorption.

To study the influence of the annealing temperature on the crystal phase and structural properties of $\text{Sb}_2(\text{S}, \text{Se})_3$ thin films, we measured the X-ray diffraction (XRD) patterns of the films

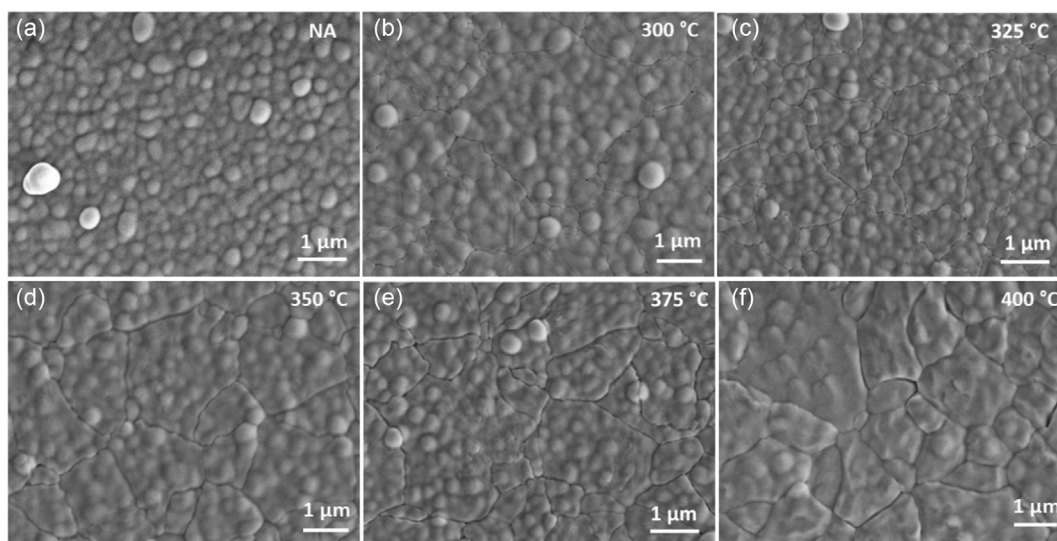


Figure 1. Top-view scanning electron microscopic (SEM) images of $\text{Sb}_2(\text{S}, \text{Se})_3$ thin films: a) without annealing and annealed at different temperatures: b) 300 °C, c) 325 °C, d) 350 °C, e) 375 °C, and f) 400 °C.

(Figure 2). The XRD pattern of the hydrothermally grown $\text{Sb}_2(\text{S}, \text{Se})_3$ film is amorphous in nature (Figure 2a). After annealing, the $\text{Sb}_2(\text{S}, \text{Se})_3$ films are converted from amorphous to the stibnite crystal structure phase (space group: Pbnm). The total peak intensity of the characteristic peaks indexed to $\text{Sb}_2(\text{S}, \text{Se})_3$ phase increases with increasing annealing temperature. The characteristic XRD peak locations show insignificant changes with annealing temperature (Table S1, Supporting Information), indicating negligible differences in the S:Se ratio, consistent with the unchanged optical bandgap (Figure S3, Supporting Information). $\text{Sb}_2(\text{S}, \text{Se})_3$ films annealed at 400 °C exhibit the highest XRD peak intensity among all tested samples, indicating the highest crystallinity. The crystallite size of the $\text{Sb}_2(\text{S}, \text{Se})_3$ was estimated by using the Debye–Scherrer equation^[18]

$$D = \frac{K\lambda}{\beta \cos \theta} \quad (1)$$

where D is the crystallite size, $K=0.9$ is the shape factor, $\lambda = 0.154$ nm is the wavelength of the X-ray, β is the full width at half maximum (FWHM), and θ is the Bragg's diffraction angle. The average crystallite size is found to be 17.3, 18.6, 22.3, 27.1, and 40.9 nm for the $\text{Sb}_2(\text{S}, \text{Se})_3$ films annealed at 300, 325, 350, 375, and 400 °C, respectively (Figure S4, Supporting Information). The trend of increasing crystallite size with increasing the annealing temperature agrees with the microstructural changes observed in the SEM images (Figure 1).

We further analyze the crystal orientation of the $\text{Sb}_2(\text{S}, \text{Se})_3$ films annealed at different temperatures by comparing the relative intensity of various characteristic XRD peaks with the most intense (120) peak. Figure 2b shows that the $\text{Sb}_2(\text{S}, \text{Se})_3$ film annealed at 350 °C has more crystalline grains in the preferred [hkl, $l \neq 0$] orientations (i.e., [211] and [221]) compared with films annealed at lower or higher temperatures. The vertically oriented grains are beneficial for charge carrier transport and extraction. For the film annealed at 400 °C, although it has higher crystallinity and larger grain size than the 350 °C annealed film, it suffers from inferior charge transport and extraction properties due to the undesired horizontal [hk0] grain orientations.

To evaluate the impact of annealing temperature on the performance of PV devices, we fabricated a series of $\text{Sb}_2(\text{S}, \text{Se})_3$ solar cells

in a superstrate configuration following the procedure illustrated in Figure S1, Supporting Information. Figure S5, Supporting Information, shows a cross-sectional SEM image of an $\text{Sb}_2(\text{S}, \text{Se})_3$ solar cell, which consists of a thin-film stack fabricated on a fluorine-doped tin oxide (FTO) coated glass superstrate, including a CdS emitter, an $\text{Sb}_2(\text{S}, \text{Se})_3$ absorber, a 2,2',7,7'-Tetrakis[N,N-di(4-methoxyphenyl)amino]-9,9'-spirofluorene (spiro-OMeTAD) hole-transport layer, and an Au back contact. Figure 3a,b compares the current density–voltage (J – V) and the external quantum efficiency (EQE) curves of the champion $\text{Sb}_2(\text{S}, \text{Se})_3$ solar cells annealed at different temperatures. The corresponding PV parameters are summarized in Table 1. The best PCE of 8.48% was obtained in the cell annealed at 350 °C. The values of short-circuit current density (J_{SC}), open-circuit voltage (V_{OC}), fill factor (FF), series resistance (R_{S}), and shunt resistance (R_{SH}) are 20.44 mA cm⁻², 670 mV, 62.06%, 3.72 Ω cm², and 642 Ω cm², respectively. Figure 3c–f shows the statistical distribution of PV parameters of devices prepared at different temperatures. The cells annealed at the optical temperature of 350 °C show significantly higher PV parameters than the devices annealed at other temperatures. The EQE value of the device annealed at 350 °C is higher in all wavelength ranges than that of others. The enhanced PV performance is mainly attributed to the improved film quality with better crystallinity, crystal orientation, and morphology, as verified by the XRD and SEM analyses. The inferior performance of the devices annealed at lower temperatures (300 and 325 °C) is likely caused by lower crystallinity, undesired grain orientation, and higher recombination compared with the target device annealed at 350 °C. The EQE curves of the low-temperature annealed devices (300 and 325 °C) exhibit an overall downward slope at wavelengths longer than 400 nm (Figure 3b), indicating very poor crystallinity and low diffusion length of the absorber layer. In contrast to the low temperature (<350 °C) annealed samples, the devices annealed at a high temperature (400 °C) show a higher J_{SC} , but suffer from more severe recombination and shunting, likely caused by the microcracks, pinholes, and undesired crystal orientation.

Annealing time is also a critical factor that dictates the PV performance of hydrothermally grown $\text{Sb}_2(\text{S}, \text{Se})_3$ solar cells. We fabricated a series of devices with different annealing temperatures (300, 350, 400 °C) and times (5–15 min), their results

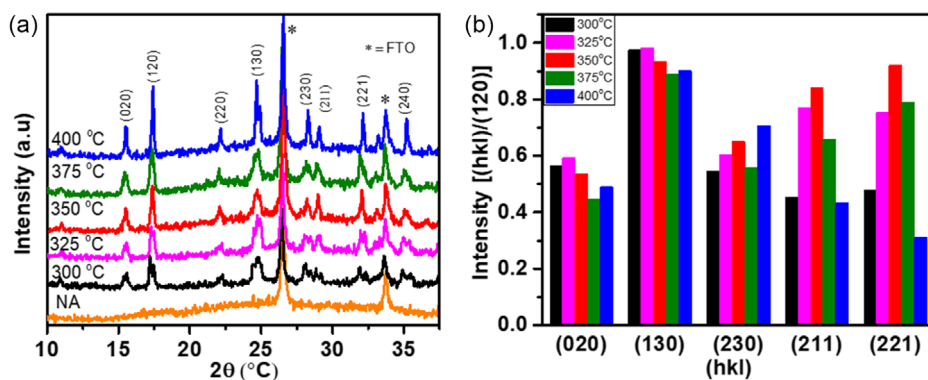


Figure 2. a) X-Ray diffraction (XRD) patterns of $\text{Sb}_2(\text{S}, \text{Se})_3$ thin films without annealing and annealed at different temperatures. b) Crystal orientation analysis for various characteristic XRD peaks of $\text{Sb}_2(\text{S}, \text{Se})_3$ films annealed at different temperatures.

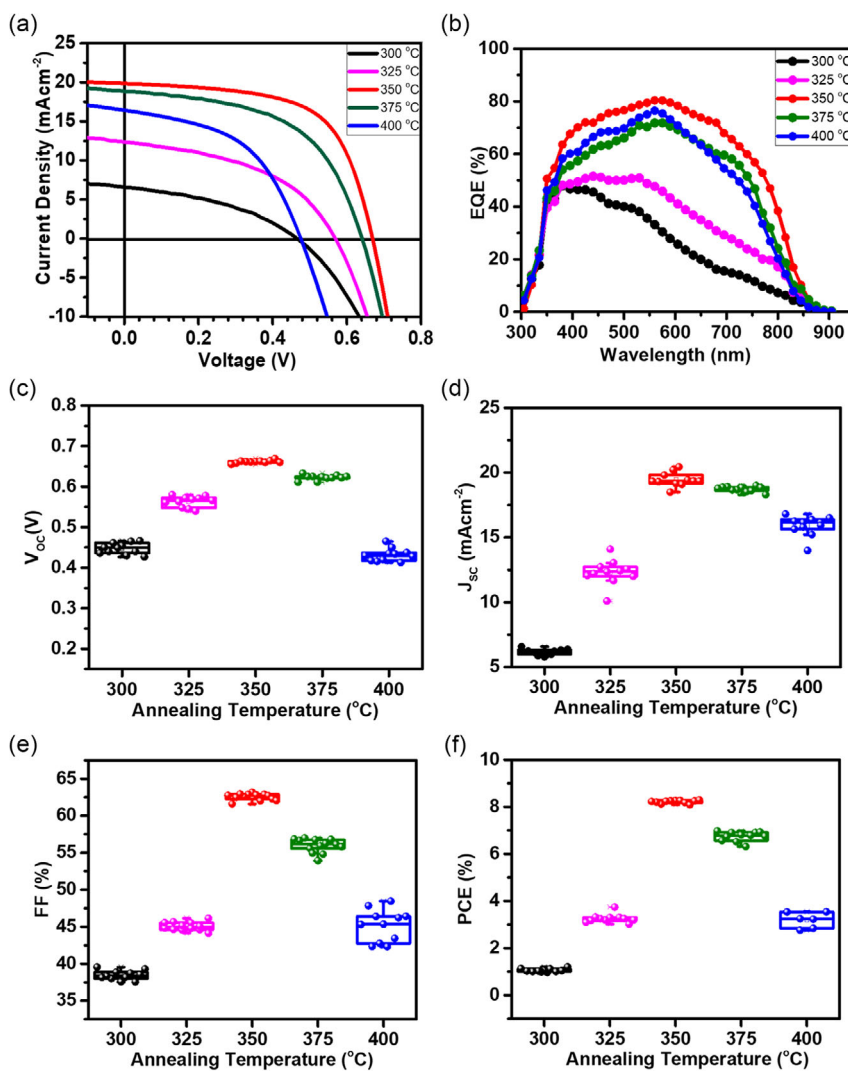


Figure 3. a) J - V and b) external quantum efficiency (EQE) curves of champion $\text{Sb}_2(\text{S}, \text{Se})_3$ solar cells annealed at different temperatures. Statistical distributions of: c) V_{OC} , d) J_{SC} , e) fill factor (FF), and f) power conversion efficiency (PCE) of $\text{Sb}_2(\text{S}, \text{Se})_3$ solar cells prepared at different annealing temperatures.

Table 1. J - V parameters of champion $\text{Sb}_2(\text{S}, \text{Se})_3$ solar cells annealed at different temperatures.

Annealing temperature [°C]	V_{OC} [mV]	J_{SC} [mA cm^{-2}]	FF [%]	PCE [%]	R_{S} [$\Omega \text{ cm}^{-2}$]	R_{SH} [$\Omega \text{ cm}^{-2}$]
300	466	6.57	39.3	1.20	31.4	229.5
325	569	12.36	45.5	3.20	14.1	281.2
350	670	20.44	62.1	8.48	3.7	642.8
375	633	18.66	56.5	6.67	8.7	428.2
400	468	16.95	48.4	3.84	17.2	171.9

are summarized in Figure S6 and Table S2, Supporting Information. When $\text{Sb}_2(\text{S}, \text{Se})_3$ was annealed at a low temperature of 300 °C, a longer annealing time (15 min) resulted in better device performance, likely due to improved crystallinity and suppressed defects. In contrast, when $\text{Sb}_2(\text{S}, \text{Se})_3$ was annealed at a

high temperature of 400 °C, a shorter annealing time (5 min) resulted in better device performance, likely due to less decomposition and shunting. For the optimal annealing temperature (350 °C), a mediate annealing time of 10 min led to the best PV performance. It is also worth noting that the $\text{Sb}_2(\text{S}, \text{Se})_3$ prepared by the facile hydrothermal method and annealed at the target temperature shows a narrow statistical distribution in PV performance. Our undergraduate and high school student researchers can reproduce efficient $\text{Sb}_2(\text{S}, \text{Se})_3$ thin-film solar cells following the same fabrication procedures (Figure S7, Supporting Information).

To better understand the origins of device performance enhancement by optimizing the annealing temperature, we selected three representative devices prepared at low (300 °C), target (350 °C), and high (400 °C) temperatures (refer to as Samples A, B, C, respectively, thereafter) for a detailed study. The defect properties of the $\text{Sb}_2(\text{S}, \text{Se})_3$ solar cells were studied by using temperature-dependent

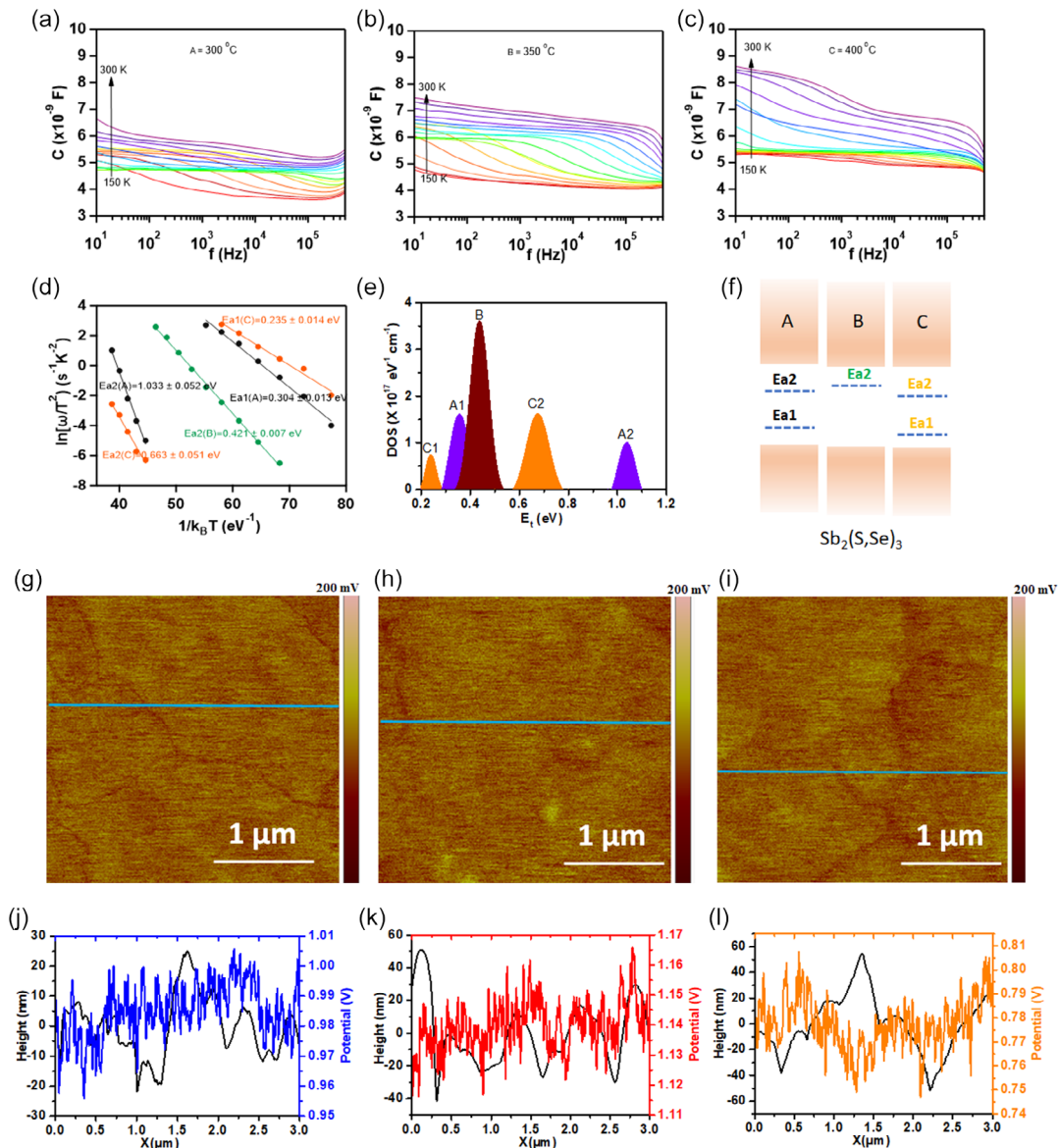


Figure 4. Temperature-dependent admittance spectra of $\text{Sb}_2(\text{S}, \text{Se})_3$ solar cells annealed at different temperatures: a) 300, b) 350, and c) 400 °C. d) Arrhenius plot for defect energy calculation. e) Calculated density of defect states for the devices. f) Schematic diagram of defect energy levels in $\text{Sb}_2(\text{S}, \text{Se})_3$ annealed at different temperatures. Images are flattened by a zero-order process to show the best contrast. g–l) Kelvin probe force microscopy (KPFM) analysis of the $\text{Sb}_2(\text{S}, \text{Se})_3$ films annealed at different temperatures: g) 300 °C, h) 350 °C, and i) 400 °C. j–l) Corresponding height profile and surface potential of the films at different temperatures.

admittance spectroscopy (TAS) in a temperature range from 150 to 300 K. **Figure 4a–c** shows the temperature-dependent capacitance–frequency (c - f) spectra of the devices. The thermal activation energy is calculated by using the following equation

$$\omega_0 = A_0 T^2 \exp \left[\frac{E_a}{k_B T} \right] \quad (2)$$

where ω_0 is the characteristic transition frequency, T is the absolute temperature, k_B is the Boltzmann constant, A_0 is a pre-exponential factor independent of temperature, and E_a is the activation energy of a signature defect seen in admittance spectroscopy.

The characteristic transition frequency at each temperature is identified by analyzing the derivative of capacitance with respect to frequency (Figure S8, Supporting Information). By fitting the Arrhenius plots in Figure 4d, we obtain two activation energies, $E_{a1}(\text{A}) = 0.304 \pm 0.013$ eV and $E_{a2}(\text{A}) = 1.033 \pm 0.052$ eV for the sample annealed at 300 °C and $E_{a1}(\text{C}) = 0.235 \pm 0.014$ eV, $E_{a2}(\text{C}) = 0.663 \pm 0.051$ eV for the sample annealed at 400 °C. In contrast, there is only one activation energy $E_{a2}(\text{B}) = 0.421 \pm 0.007$ eV for the samples annealed at 350 °C. Figure 4e plots the density of states for each defect level calculated based on the TAS curves. We also perform capacitance–voltage (C–V) measurement and Mott–Schottky analysis on three

representative devices. Among them, the target device annealed at 350 °C shows the lowest apparent carrier density and longest depletion width (Figure S9, Supporting Information). The capacitance measurement results reveal that annealing an Sb₂(S, Se)₃ film at the target temperature of 350 °C can suppress defect formation, likely ascribed to the increased crystallinity combined with more preferred crystal orientations. Yet, the relatively deep defect level (≈ 0.4 eV) and a high defect density on the order of $\approx 10^{17}$ cm⁻³ still limit the V_{OC}-deficit of Sb₂(S, Se)₃ solar cells to ≈ 670 mV, corresponding to a high open-circuit voltage deficit of ≈ 0.8 V.

Since the antimony atom requires a much higher temperature than chalcogenide to reach the same partial vapor pressure (e.g., Sb at 807 K vs S/Se at 375/500 K for 1 Pa), the Sb₂(S, Se)₃ films annealed at an elevated temperature (>573 K) are expected to show an Sb-rich and (S, Se)-poor stoichiometry and slightly n-type doping. The energy-dispersive spectroscopy (EDS) measurements confirm the Sb-rich and (S, Se)-poor stoichiometry for all annealed Sb₂(S, Se)₃ films (Figure S10 and Table S3, Supporting Information). As a result, these calculated defect activation energies can be tentatively assigned as antimony antisites (Sb_{S_{Se}} and Sb_S) and chalcogenide vacancies (V_S and V_{Se}) and allocated to their corresponding energy levels in the band diagram (Figure 4f). However, it is intricate to distinguish these defects due to the complexity of the defect physics of Sb₂(S, Se)₃. Nonetheless, the defects with deeper activation energies have more chances to act as nonradiative recombination centers. The sample annealed at the target temperature of 350 °C has a relatively shallower activation energy level than the samples annealed at higher or lower temperatures, indicating that some of the deeper defects are completely or partially passivated or become shallower. The lower defect activation energy of the target sample annealed at 350 °C enables a higher device performance than others.

To further analyze the impact of defect levels on the Fermi energy of Sb₂(S, Se)₃ films annealed at different temperatures, we performed Kelvin probe force microscopy (KPFM) measurements (Figure 4g–i). The average surface potential of Sb₂(S, Se)₃ films annealed at 300, 350, and 400 °C are found to be around 0.99, 1.14, and 0.79 V, respectively. The film annealed at 350 °C shows a higher surface potential than films annealed at higher or lower temperatures, corresponding to a shallower Fermi energy (closer to the vacuum level) and higher n-type doping at the surface. The Fermi energy levels of the Sb₂(S, Se)₃ films annealed at different temperatures are in agreement with the defect levels shown in Figure 4f. The shallower Fermi energy in the 350 °C annealed film could be attributed to higher densities of antimony antisites and chalcogenide vacancies, as revealed by the TAS measurement (Figure 4e). The more pronounced chalcogenide deficiency in the 350 °C annealed film is likely responsible for the higher n-type doping at the surface. The shallower work function of Sb₂(S, Se)₃ is beneficial for achieving quasi-Fermi energy of electrons closer to the conduction band, enabling a higher V_{OC} of a solar cell.

3. Conclusions

In conclusion, we investigated the impact of post-annealing temperature on the PV performance of hydrothermally grown

Sb₂(S, Se)₃ solar cells. We found that the annealing temperature of 350 °C was beneficial to increasing the grain size, crystallinity, crystal orientation, and compactness of the films. After optimizing the annealing process, we obtained Sb₂(S, Se)₃ solar cells with an improved PCE from 1.20 to 8.48% and investigated the interplay between defects and solar cell performance. Our results show that hydrothermal growth followed by proper annealing is a promising approach to fabricating efficient Sb₂(S, Se)₃ thin-film solar cells.

4. Experimental Section

Device Fabrication: The Sb₂(S, Se)₃ thin films were deposited onto the CdS-coated FTO glass substrates by a hydrothermal method. The CdS layer was first deposited by a CBD approach, following the previously reported method.^[19] Afterward, the obtained CdS film was annealed in ambient air at 400 °C for 10 min. For the Sb₂(S, Se)₃ deposition, potassium antimony tartrate (C₈H₄K₂O₁₂Sb₂·3H₂O), sodium thiosulfate pentahydrate (Na₂S₂O₃·5H₂O), and selenourea (CH₄N₂Se) were used as Sb, S, and Se sources, respectively. 20 mm of C₈H₄K₂O₁₂Sb₂·3H₂O, 40 mm of Na₂S₂O₃·5H₂O, and 35 mg of CH₄N₂Se were mixed in 50 mL of DI water.^[13b] The mixed solution was stirred until it turned clear and homogeneous faint yellowish. Then, the solution was transferred into the cleaned inner Teflon tank of an autoclave. During the synthesis, the substrate was placed in such a way that the CdS layer faced downward. Finally, the tight autoclave with the solution was kept in an oven heated at 130 °C for 3 h.

The autoclave was taken out of the oven and allowed to cool to room temperature. The films were then taken out from the autoclave and dried by blowing N₂ gas. Afterward, the films were loaded inside the tube furnace on the graphite plate, and the tube was vacuumed till we got a pressure of 3 mT. Then, we annealed the samples in two-step processes. First, we heated the graphite plate, which holds the samples, at 100 °C using the IR heater from the top and bottom sides for one minute. This first step of heating is done to remove the water or any other solvent remaining on the film. Then finally, we filled the tube with 10 Torr of N₂ gas and heated the films at different temperatures from 300 to 400 °C for 10 min. After 10 min of heating, the films were allowed to cool down to room temperature.

Finally, we prepared a device in a superstrate configuration: FTO/CdS/Sb₂(S, Se)₃/Spiro-OMeTAD/Au. We used Tec-12D FTO glass substrate from Pilkington North America Inc. The Spiro-OMeTAD was used as a hole transport layer (HTL). HTL solution was made by a Spiro-OMeTAD (Lumtec)/chlorobenzene (91 mg/1 mL) solution with an additive of 21 μ L of Li-bis(trifluoromethanesulfonyl) imide (Li-TFSI)/acetonitrile (540 mg/1 mL), 35 μ L of 4-tert-butylpyridine (TBP) and 9 μ L of tris(2-(1H-pyrazol-1-yl)-4-tert-butylpyridine)-cobalt(III) tris(bis(trifluoromethylsulfonyl)imide (FK 209)/acetonitrile (376 mg/1 mL). After that, a spiro-OMeTAD film was spin-coated on the Sb₂(S, Se)₃ film at a speed of 2500 rpm for 30 s then the film was left overnight to get oxidized. Finally, Au was deposited on the top of Spiro as a back contact electrode using a thermal evaporator under a pressure of 5×10^{-6} Torr. The active area of each cell is 0.08 cm².

Device Characterization: Sb₂(S, Se)₃ film morphology was characterized by using high-resolution field emission scanning electron microscopy (FE-SEM, Hitachi S-4800) equipped with X-ray energy dispersive spectroscopy (EDS). X-ray diffraction (XRD, Rigaku Ultima III, Cu K α radiation under operation conditions of 40 kV and 44 mA) was used to study the crystal properties of the Sb₂(S, Se)₃ films. The performance of the Sb₂(S, Se)₃ solar cells was measured using J–V curves under AM1.5G illumination using a LED solar simulator (Newport) and a source meter (Keithley 2400) at a scanning speed of 1.17 versus QE system (PV Measurements) was used to measure the EQE spectra. Home-built KPFM was used to measure the KPFM which is based on the D3100 atomic force microscope (AFM). Pt–Ir-coated silicon probes (Nano sensor PPP-EFM) were used in the KPFM measurement. The scan size was $5 \times 5 \mu$ m² that contained 1024 \times 256 pixels. Modulab potentiostat equipped with a frequency response analyzer (Ametek Inc.) was used for the C–V and TAS measurements. Modulab system was used to set

up, run experiments, and obtain the results with the help of inbuilt XM-studio software. A constant AC modulation voltage of 45 mV_{rms} was used for C–V and TAS measurements. The C–V measurements were performed in the dark with a 10 kHz AC signal superimposed on a DC bias voltage varying from –2 to 0.8 V. For the TAS measurements, there was a frequency sweeping from 1.0 MHz to 0.1 Hz. To carry out all the temperature-dependent measurements, a liquid-nitrogen-cooled cryogenic system (Janis VPF-100) was used. The temperature was controlled using a temperature controller (Lakeshore 330). A temperature sensor was mounted directly on the top of the device to get the actual temperature of the samples.

Supporting Information

Supporting Information is available from the Wiley Online Library or from the author.

Acknowledgements

This material is based on research sponsored by the U.S. Air Force Research Laboratory under agreement numbers FA9453–19-C-1002 and FA9453-21-C-0056. This work is authored in part by the National Renewable Energy Laboratory (NREL), operated by the Alliance for Sustainable Energy for the US Department of Energy (DOE) under contract no. DE-AC36-08GO28308. The views and conclusions contained herein are those of the authors and should not be interpreted as necessarily representing the official policies or endorsements, either expressed or implied, of the U.S. Air Force Research Laboratory or the U.S. Government. Public Affairs release approval #AFRL-2022-5114. This work was supported by the National Science Foundation under contract no. DMR-1807818. The authors also thank the National Science Foundation for funding through the grant Research Experiences for Undergraduates #1950785. A.E. and A.P. acknowledge the support of the University of Toledo's Research In Science & Engineering (RISE) program.

Conflict of Interest

The authors declare no conflict of interest.

Data Availability Statement

The data that support the findings of this study are available from the corresponding author upon reasonable request.

Keywords

annealing, antimony sulfoselenide, defects, hydrothermal growth, thin-film solar cells

Received: November 7, 2022

Revised: November 28, 2022

Published online: December 22, 2022

- [1] NREL, Best Research-Cell Efficiency Chart, <https://www.nrel.gov/pv/cell-efficiency.html> (accessed: October 2022).
- [2] M. Nakamura, K. Yamaguchi, Y. Kimoto, Y. Yasaki, T. Kato, H. Sugimoto, *IEEE J. Photovoltaics* **2019**, *9*, 1863.
- [3] <https://www.ise.fraunhofer.de/content/dam/ise/de/documents/publications/studies/Photovoltaics-Report.pdf> (accessed: October 2022).
- [4] K. Zeng, D.-J. Xue, J. Tang, *Semicond. Sci. Technol.* **2016**, *31*, 063001.
- [5] H. J. T. Nkuissi, F. K. Konan, B. Hartiti, J.-M. Ndjaka, in *Reliability and Ecological Aspects of Photovoltaic Modules*, IntechOpen, London, United Kingdom **2020**.
- [6] a) S. Rijal, D.-B. Li, R. A. Awni, S. S. Bista, Z. Song, Y. Yan, *ACS Appl. Energy Mater.* **2021**, *4*, 4313; b) S. Rijal, D. B. Li, R. A. Awni, C. Xiao, S. S. Bista, M. K. Jamarkattel, M. J. Heben, C. S. Jiang, M. Al-Jassim, Z. Song, Y. Yan, *Adv. Funct. Mater.* **2021**, *32*, 2110032.
- [7] Y. Zhou, L. Wang, S. Chen, S. Qin, X. Liu, J. Chen, D.-J. Xue, M. Luo, Y. Cao, Y. Cheng, *Nat. Photonics* **2015**, *9*, 409.
- [8] a) R. Tang, X. Wang, W. Lian, J. Huang, Q. Wei, M. Huang, Y. Yin, C. Jiang, S. Yang, G. Xing, *Nat. Energy* **2020**, *5*, 587; b) N. K. Jayswal, S. Rijal, B. Subedi, I. Subedi, Z. Song, R. W. Collins, Y. Yan, N. J. Podraza, *Sol. Energy* **2021**, *228*, 38.
- [9] a) Y. Zhou, M. Leng, Z. Xia, J. Zhong, H. Song, X. Liu, B. Yang, J. Zhang, J. Chen, K. Zhou, J. Han, Y. Cheng, J. Tang, *Adv. Energy Mater.* **2014**, *4*, 1301846; b) X. Wang, R. Tang, Y. Yin, H. Ju, S. A. Li, C. Zhu, T. Chen, *Sol. Energy Mater. Sol. Cells* **2019**, *189*, 5.
- [10] Y. Pan, X. Hu, Y. Guo, X. Pan, F. Zhao, G. Weng, J. Tao, C. Zhao, J. Jiang, S. Chen, *Adv. Funct. Mater.* **2021**, *31*, 2101476.
- [11] a) R. Tang, Z.-H. Zheng, Z.-H. Su, X.-J. Li, Y.-D. Wei, X.-H. Zhang, Y.-Q. Fu, J.-T. Luo, P. Fan, G.-X. Liang, *Nano Energy* **2019**, *64*, 103929; b) X. Liang, X. Chen, Z. Li, G. Li, J. Chen, L. Yang, K. Shen, Y. Xu, Y. Mai, *Appl. Phys. A* **2019**, *125*, 381.
- [12] M. Calixto-Rodriguez, H. M. Garcia, M. T. S. Nair, P. K. Nair, *ECS J. Solid State Sci. Technol.* **2013**, *2*, Q69.
- [13] a) X. Wang, R. Tang, C. Jiang, W. Lian, H. Ju, G. Jiang, Z. Li, C. Zhu, T. Chen, *Adv. Energy Mater.* **2020**, *10*, 2002341; b) W. Wang, X. Wang, G. Chen, L. Yao, X. Huang, T. Chen, C. Zhu, S. Chen, Z. Huang, Y. Zhang, *Adv. Electron. Mater.* **2019**, *5*, 1800683.
- [14] S. Rijal, Z. Song, D. B. Li, S. S. Bista, Y. Yan, *presented at 2021 IEEE 48th Photovoltaic Specialists Conf. (PVSC)*, IEEE, Fort Lauderdale, FL, USA, June 2021.
- [15] Y. Zhao, S. Wang, C. Jiang, C. Li, P. Xiao, R. Tang, J. Gong, G. Chen, T. Chen, J. Li, X. Xiao, *Adv. Mater.* **2022**, *12*, 2103015.
- [16] G.-J. Chen, R. Tang, S. Chen, Z.-H. Zheng, Z.-H. Su, H.-L. Ma, X.-H. Zhang, P. Fan, G.-X. Liang, *ACS Appl. Mater. Interfaces* **2022**, *14*, 31986.
- [17] C. Gao, J. Huang, H. Li, K. Sun, Y. Lai, M. Jia, L. Jiang, F. Liu, *Ceram. Int.* **2019**, *45*, 3044.
- [18] D. Pokhrel, E. Bastola, K. Khanal Subedi, S. Rijal, M. K. Jamarkattel, R. A. Awni, A. B. Phillips, Y. Yan, M. J. Heben, R. J. Ellingson, *Sol. Energy Mater. Sol. Cells* **2022**, *235*, 111451.
- [19] D.-B. Li, X. Yin, C. R. Grice, L. Guan, Z. Song, C. Wang, C. Chen, K. Li, A. J. Cimaroli, R. A. Awni, D. Zhao, H. Song, W. Tang, Y. Yan, J. Tang, *Nano Energy* **2018**, *49*, 346.